

PAPER • OPEN ACCESS

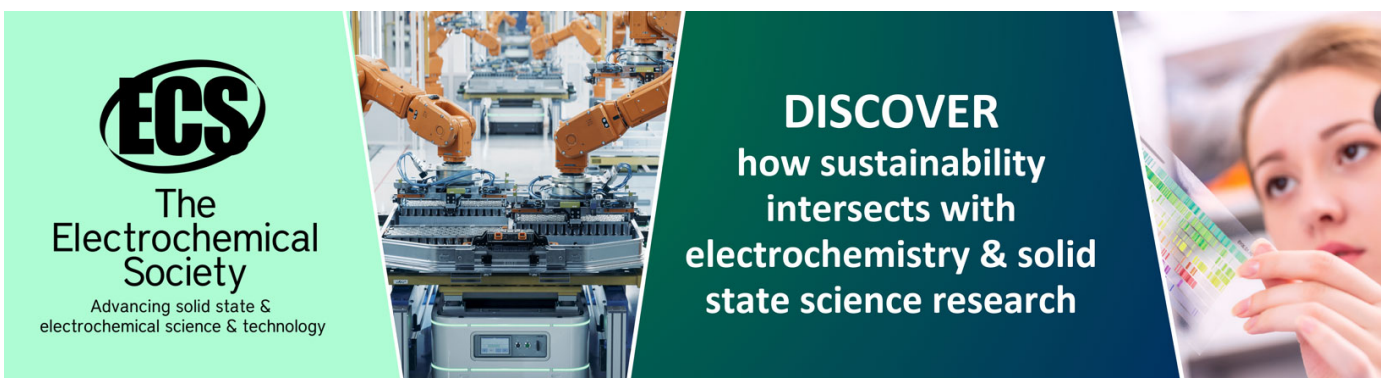
One-step synthesis of strongly confined, defect-free and hydroxy-terminated ZnO quantum dots

To cite this article: Gunisha Jain *et al* 2020 *Nanotechnology* **31** 215707

View the [article online](#) for updates and enhancements.

You may also like

- [The quantum confined Stark effect in N-doped ZnO/ZnO/N-doped ZnO nanostructures for infrared and terahertz applications](#)
Pornsawan Sikam, Roohan Thirayatom, Pairoot Moontragoon *et al.*
- [Stability of ZnO quantum dots tuned by controlled addition of ethylene glycol during their growth](#)
Lizandra M Zimmermann, Paulo V Baldissera and Ivan H Bechtold
- [The structure and optical properties of ZnO nanocrystals embedded in SiO₂ fabricated by radio-frequency sputtering](#)
G Mayer, M Fonin, U Rüdiger *et al.*



ECS
The
Electrochemical
Society
Advancing solid state &
electrochemical science & technology

DISCOVER
how sustainability
intersects with
electrochemistry & solid
state science research

One-step synthesis of strongly confined, defect-free and hydroxy-terminated ZnO quantum dots

Gunisha Jain , Conor Rocks, Paul Maguire and Davide Mariotti

Nanotechnology and Integrated Bioengineering centre, Ulster University, Newtownabbey, United Kingdom

E-mail: jaingunisha@gmail.com

Received 2 September 2019, revised 1 January 2020

Accepted for publication 4 February 2020

Published 10 March 2020



CrossMark

Abstract

This paper reports the production of strongly confined ligand-free, defect-free, hydroxy-terminated ZnO quantum dots with a mean diameter of 1.9 nm, by radio frequency atmospheric pressure microplasma. Systematic characterization is performed to understand the surface chemistry of ZnO quantum dots. Photoluminescence studies show strong confinement effect on emission with only ultraviolet (UV) emission without any defect-related visible emission. Emission is again tested after eighteen months and confirms the QDs long-term emission stability. The mechanism responsible for this UV emission is also discussed and originates from OH-related surface terminations.

Keywords: hydroxy-terminated ZnO quantum dots, quantum confinement, band alignment, photoluminescence, defect-free

(Some figures may appear in colour only in the online journal)

1. Introduction

Zinc oxide (ZnO) has always been of great interest because of its application in various technologies such as ultra-violet (UV) lasers [1, 2], photovoltaics (used as a transparent and conductive layer) [3–6], light-emitting diodes [7] and electroluminescence devices [8]. ZnO has a wide bandgap (~ 3.3 eV) with large exciton binding energy (~ 60 meV), optical transparency, electric conductivity and piezoelectric properties. It is also of great interest due to reduced toxicity and limited environmental impact compared to other II–VI semiconductors. Its n-type nature makes it highly suitable as an electron acceptor or transparent electrode often as a competitor to materials such as TiO_2 . Among the different ZnO nanostructures (e.g. nanowire, nanoneedles, nanoflowers), zero-dimensional ZnO quantum dots (QDs) have strong impact on optoelectronic properties. Three-

dimensional quantum confinement of carriers can improve the optoelectronic properties of ZnO QDs by increasing carrier life-time and enhancing photoluminescence. However, controlling these properties is challenging because these are determined by defects such as oxygen/zinc vacancies and interstitials [9]. QDs are unique in this respect because they are less prone to deeper structural defects and tend to segregate defects at the surface. However, at the same time, the impact of surface defects is stronger than in bulk and understanding their resultant complex optoelectronic properties can be difficult. It has been observed for instance that quantum confined systems can enhance excitonic emission from ZnO but still have surface defects related emissions [10]. Because defects are at the surface, they can be easily accessed, and passivation strategies can offer opportunities for controlling as well as tuning these properties, particularly emission properties [11, 12], higher stability and resistivity toward oxygen and water with the additional advantage of bandgap tunability [13]. Most often synthesis and passivation represent two separate steps in the preparation of nanoparticles; however, plasma-based synthesis can provide avenues for synthesizing nanoparticles with appropriate



Original content from this work may be used under the terms of the [Creative Commons Attribution 4.0 licence](https://creativecommons.org/licenses/by/4.0/). Any further distribution of this work must maintain attribution to the author(s) and the title of the work, journal citation and DOI.

passivation in a one-step process. For instance, Felbier *et al* [14] reported ZnO QDs synthesis by low-pressure radio-frequency (RF) plasma using diethylzinc and oxygen gas as precursors. On the other hand, atmospheric pressure plasmas (APPs) have gained substantial attention due to the possibility of low-cost, flexible and highly versatile processes.

Here, we report defect-free and hydroxy-passivated ZnO QDs synthesized by radio-frequency (RF) APPs. Compared to other methods which use metal-organic and other expensive chemical compounds, we have synthesized ZnO QDs directly from a high purity metallic zinc wire, as Zn precursor, and environmental oxygen. This approach offers clear advantages in the management of precursor and process gases and represents a very simple and quick synthesis method for ZnO QDs. Furthermore, this process has allowed us to achieve ZnO QDs with unique characteristics never reported before. We have synthesized QDs with a mean diameter of 1.9 nm where active oxygen defects at the surface are passivated during growth introducing hydroxyl groups [15–17]. ZnO QDs synthesized with this method are therefore within the strong quantum confinement regime (determined by the Bohr radius, 0.9–2.34 nm for ZnO) [14, 18–23] and where defects have been eliminated also at the surface with effective OH-passivation in a single step process.

2. Experimental details

The plasma system consists of a stainless steel (SS) tube with a quartz capillary (1 mm outer diameter and 0.7 mm internal diameter) containing a 99.99% pure zinc wire (Alfa Aesar) of 0.25 mm diameter and around it a copper powered electrode, as shown in figure 1. The zinc wire acts as ground electrode through the grounded SS capillary tube. Radio frequency power (13.56 MHz) was applied to the powered electrode and argon gas was used to produce the plasma. The gas flow rate and applied power were set to 150 sccm and 40 W respectively. The plasma was generated between the powered electrode and the zinc wire. The distance between the capillary and the collector (i.e. a solid substrate or a vial with ethanol) was ~ 1.5 cm, which allows for interaction between the plasma after-glow and the atmospheric oxygen. In order to ensure the repeatability of the process, the synthesis was carried out for 30 min for each sample produced.

Transmission electron microscopy (TEM) and high-resolution TEM (HRTEM) were performed (Jeol JEM02100 F) by collecting the sample in ethanol and drop-casting on carbon-coated gold grids. The ZnO QDs were also deposited on a silicon substrate for scanning electron microscopy (SEM; FEI Quanta 200 3D). X-ray photoelectron spectroscopy (XPS; Kratos Axis Ultra DLD) of the samples on Si substrate was also carried out to identify the chemical composition using Al K_{α} radiation. XPS measurements were also used to determine the valence band-edge. Fourier transform infrared spectroscopy (FTIR; ThermoScientific iS5) was performed to gain chemical information of the ZnO QDs, also deposited on

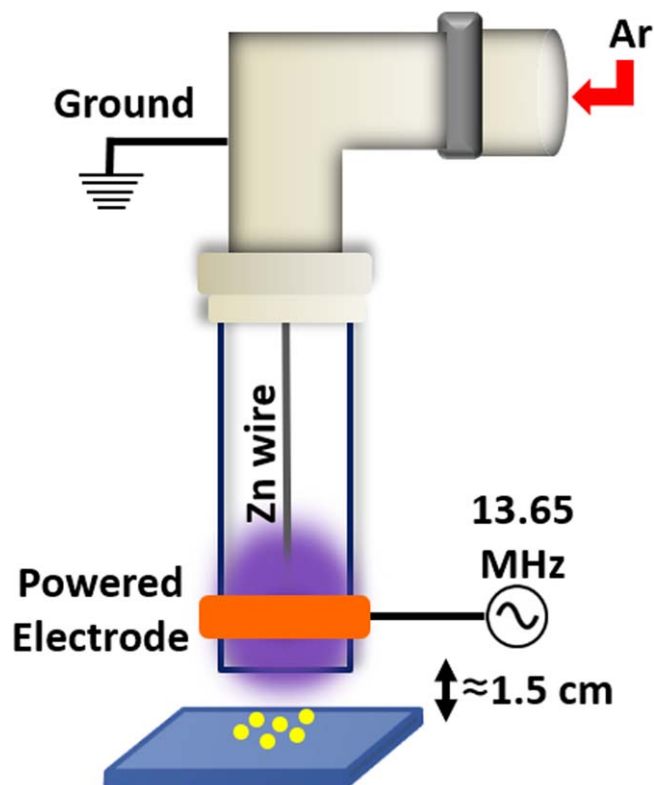


Figure 1. Experimental set-up of the RF plasma reactor used for ZnO QDs synthesis.

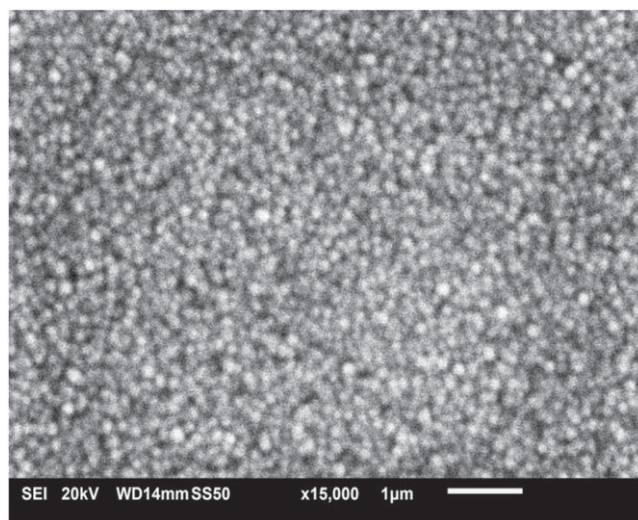


Figure 2. Scanning electron microscope image of particle deposition at 40 W with 150 sccm of Ar flow.

Si substrates. The samples were deposited on glass substrates coated with indium-doped tin-oxide to carry out Kelvin probe (SKP 4.5, KP Technology Ltd UK) measurements, to find out Fermi level of the films. Finally, we measured optical characteristics using ultraviolet-visible (UV-vis; PerkinElmer LAMBDA 365) spectroscopy by collecting ZnO QD directly in ethanol and calculated the corresponding bandgap by Tauc plot by measuring both transmission as well as reflectance/scattering. ZnO QDs colloids in ethanol were also used to

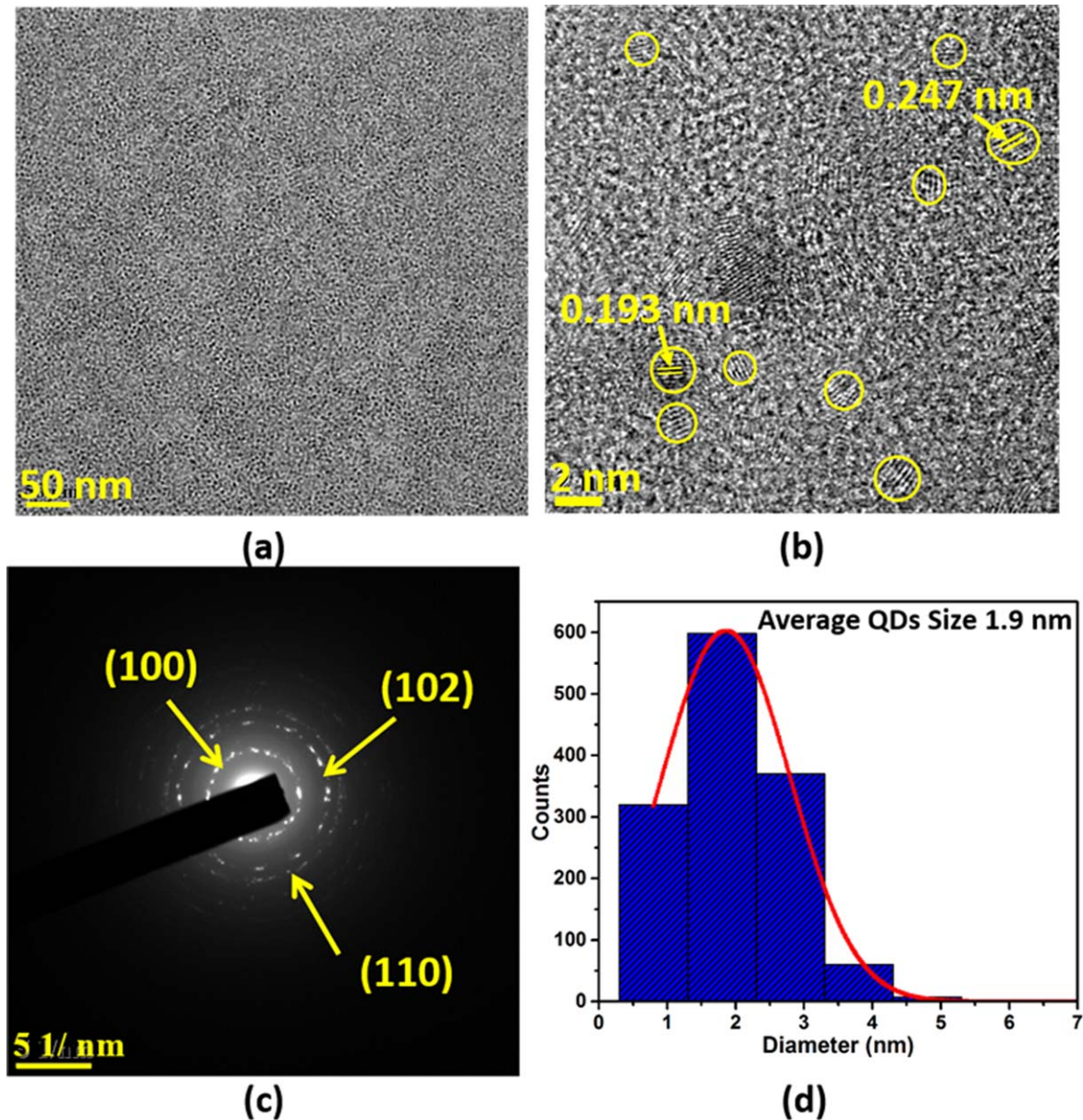


Figure 3. (a) and (b) Transmission electron microscope images of ZnO QD, (c) SAED pattern and (d) particle size analysis.

measure the photoluminescence (PL; Cary eclipse fluorescence spectrophotometer, Agilent Tech).

3. Results and discussion

A typical SEM image of the ZnO QDs deposited on a silicon substrate is shown in figure 2; this shows relatively good uniformity of the film over a micrometer range. However, the deposition process of large films is not optimized yet and, as it is often the case for this type of plasmas, films are highly porous and non-compact [24]. Of course, the resolution of the SEM is not sufficient to identify the QDs and the morphology observed in figure 2 is due to randomly oriented and agglomerated ZnO QDs when deposited directly on a

substrate; the size of the agglomerates is within the range of 50–150 nm.

TEM images have revealed the uniform size and crystalline nature of the sample as shown in figures 3(a) and (b). The inter-planar spacing was calculated and found to be 0.247 nm and 0.193 nm which is a good match with (101) and (102) planes of wurtzite ZnO (figure 3(b)), respectively. ZnO planes (100), (102) and (110) can also be observed in the SAED pattern in figure 3(c). The histogram in figure 3(d) shows the size distribution of the QDs with mean diameter of 1.9 nm.

FTIR measurements are performed in nitrogen environment and can be seen in figure 4(b). Four peaks are observed at 925 cm^{-1} , 1410 cm^{-1} , 1640 cm^{-1} and 3480 cm^{-1} in this graph. The broad band in the range of $3200\text{--}3700\text{ cm}^{-1}$ is assigned to stretching vibration of OH [25–28]. Non-bonding OH stretching appears at higher frequency near 3600 cm^{-1}

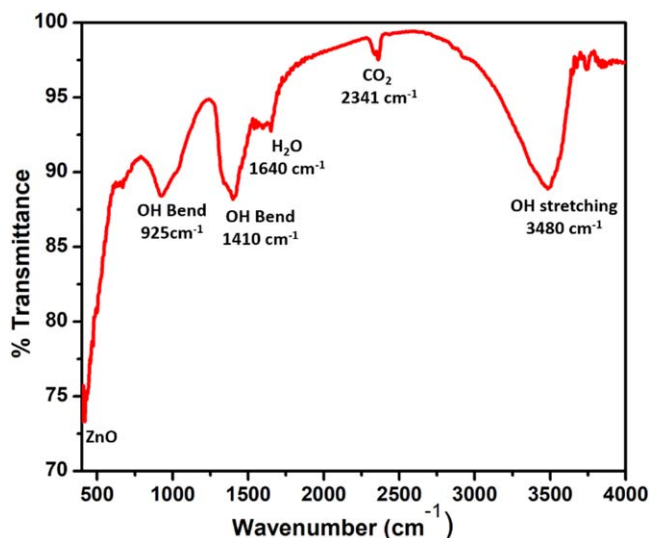


Figure 4. Fourier-transform IR spectrum of ZnO QDs, showing different OH vibration.

while inter-molecular hydrogen bonding shifts the peak to lower frequency near 3200–3550 cm^{-1} [27]. Bending vibration of OH can be seen at 1395–1440 cm^{-1} and 910–950 cm^{-1} [27–29]. Peaks at 925 cm^{-1} , 1410 cm^{-1} and 3480 cm^{-1} correspond to OH bending and stretching vibration. Bending vibration suggests the inter-molecular hydrogen bonding between OH molecules when OH is abundant [27, 28, 30]. The small peak at 1640 cm^{-1} corresponds to OH vibration in H₂O [27, 31, 32]. Specific ZnO-related peaks (~ 436 – 529 cm^{-1}) can be only observed in part as these were just outside the available range. We should note that the OH-related peaks at 925 cm^{-1} and 1410 cm^{-1} are not generally observed for adsorbed water [27, 29] and therefore suggest the presence of OH-terminations at the ZnO QD surfaces (see further below for more evidence). The small peak at 665 cm^{-1} correspond to bending vibration of CO₂ from air [33].

XPS was performed to analyze further the chemical composition and oxidation state of ZnO. Binding energy (BE) of elements was calibrated against C 1s (284.6 eV). XPS survey shows Zn and O peaks as shown in figure 5(a) and confirms ZnO formation. Binding energy at 1021.94 eV and 1045.14 eV are attributed to binding energy of Zn_{2p_{3/2}} and Zn_{2p_{1/2}} electrons as shown in figure 5(b). The BE difference between these two peaks is 23.2 eV, which is close to that reported in the literature (23.1 eV) and confirms that Zn is in the Zn⁺² state as expected for ZnO [34–36]. In the XPS spectra, the asymmetric O 1s peak was observed with a shoulder at higher binding energy. O 1s spectrum was fitted by two peaks centered at 531.74 eV and 532.88 eV (figure 5(c)). A peak in the range of 529–530.5 eV corresponds to O⁻² in Zn–O binding. However, in our samples we do not observe any peak in this range. The first peak at 531.74 eV can be ascribed to O–H groups, which is consistent with the strong FTIR signal that indicates the presence of hydroxyl groups. The higher energy peak at 532.88 eV can be attributed to adsorbed oxygen in H₂O or –CO₃ species [37, 38]. While the Zn_{2p_{3/2}} and Zn_{2p_{1/2}} peaks clearly demonstrate the

chemical composition of ZnO, we do not observe a clear contribution from Zn–O bonds in the O 1s. This may be due to much lower intensity resulting from the volume-to-surface ratio or it is possible that the peak measured at 531.74 is in fact a combination of OH as well as Zn–O, with the latter shifted due to the small size of the QDs.

To confirm further the chemical state of the ZnO QDs, zinc LMM Auger spectrum is also recorded as shown in figure 5(d). Auger peaks of metallic zinc, zinc hydroxide and zinc oxide appear at 992 eV, 986.5 eV and 988.6 eV respectively. Our recorded value at 988.9 eV is in very good agreement with the literature value for ZnO at 988.6 eV [39]. The Auger signal can be considered more reliable due to the interrogation of deeper electronic states and it provides strong evidence of the formation of ZnO.

Overall the combined material characterization of the ZnO QDs confirms the crystal structure (HRTEM and SAED) and chemical composition (FTIR, XPS). Moreover, XPS and FTIR analysis indicate the strong presence of bonded OH groups which are not to be assigned to adsorbed moisture and therefore strongly support the formation of OH-terminations. This will be further supported by PL measurements.

The difference between the Fermi level (E_f) and valance band maximum (E_{VBM}) was evaluated from the XPS spectra shown in figures 5(e) and (f). This was done by extrapolating the leading edge of the XPS spectra to the baseline as shown in the figure 5(f) and produced a value of 2.63 eV ($E_f - E_{VBM}$).

The Fermi level was then obtained by measuring the contact potential difference (CPD) between the ZnO sample and a reference electrode. The calibration of the system was carried out by measuring the work function (Φ) of a known gold reference (5.1 eV). The work function of the sample can then be calculated with:

$$\Phi_{Sample} = 5.1 - CPD_{Au} + CPD_{Sample}, \quad (1)$$

where CPD_{Au} is the contact potential difference between the Au reference and Au tip, CPD_{Sample} is the contact potential difference between sample and Au tip. On this basis, the Fermi level of our ZnO QDs was measured to be -5.57 eV, which is more negative than the Fermi level of bulk ZnO (-5.2 eV) [40]. This difference is the result of changes in charge distribution and electric environment in quantum confined systems [41, 42].

The UV–vis transmission spectrum is recorded from ZnO QDs in ethanol colloids as shown in figure 6(a). The absorption features of the direct bandgap semiconductors (such as ZnO) can be described from the following relation [43]:

$$(\alpha h\nu)^2 \propto (h\nu - E_g), \quad (2)$$

where α is the absorption coefficient, $h\nu$ is the photon energy and E_g is the bandgap of bulk. The relative value of the absorption coefficient is calculated by transmittance measurement if we assume that scattering is negligible. Figure 6(b) reports the Tauc plot according to equation (2). The linear region of the plot indicates the direct nature of the bandgap and the intercept gives a bandgap of 4.27 eV. The relationship between the bandgap and particle size can be

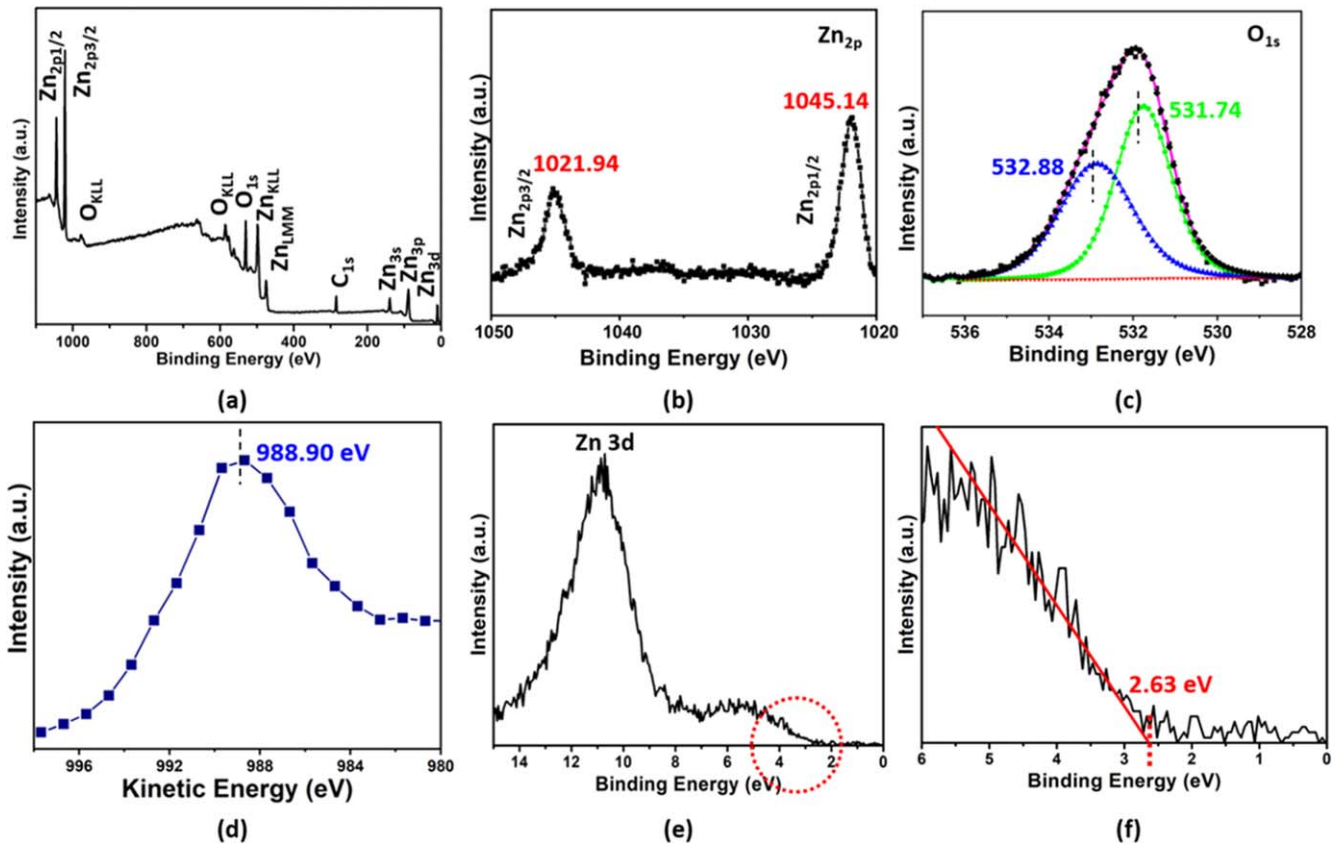


Figure 5. (a) X-ray photoelectron spectrum (XPS) survey scan of ZnO; (b) Zn 2p; (c) O 1s; (d) shows Zn LMM Auger Electron Spectra; (e) onset of the XPS spectra of ZnO and (f) shows $E_f - EVBM$.

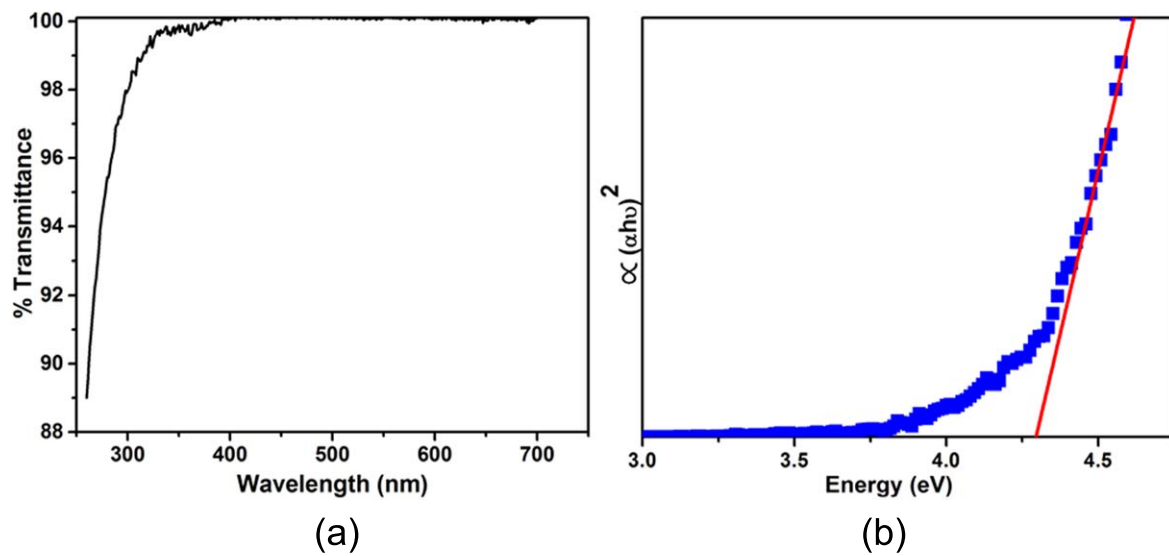


Figure 6. (a) Transmission spectrum of ZnO QDs and (b) shows Tauc plot and bandgap of ZnO.

estimated according to various theoretical models [44–46]. Changes in the ZnO bandgap follows an exponential trend and can be seen for QDs with diameters below 4 nm [46]. Our ZnO QDs are therefore expected to be in the strong confinement regime and having a large bandgap.

Here, because of the strong confinement of these particles, effective mass model for spherical particles with coulombic interaction is no more valid for bandgap calculations

[20, 21, 46]. The theoretical value of the bandgap was determined from equation (3) [46] as 4.46 eV using the mean diameter (1.9 nm) that we previously measured:

$$E^* = 3.30 + \frac{3.54}{d^{1.74}}. \quad (3)$$

Here, d is the diameter of quantum dot. The difference between theoretical and experimental values can be due to a

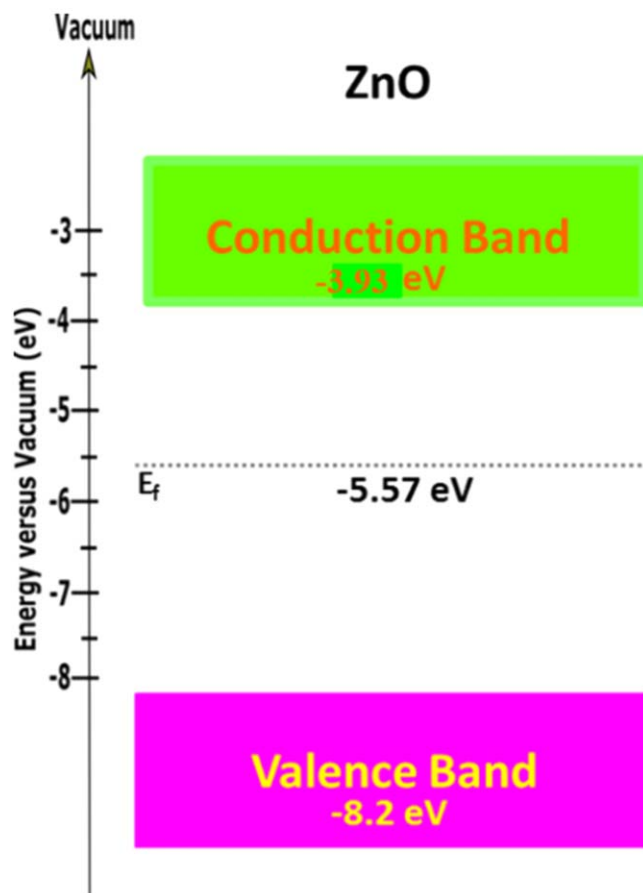


Figure 7. Estimated band alignment diagram of ZnO QDs with XPS, UV-vis and Kelvin prob analysis.

range of factors where theoretical calculations generally assume chemically unaltered surfaces with respect to the QD core [46]. However, experimentally, surface terminations are unavoidable (such as $-\text{OH}$) and are known to affect the properties of quantum confined systems [47].

The complete band structure of ZnO is depicted in figure 7. The position of the valence band edge was calculated from the XPS results ($E_f - E_{VBM} = 2.63$ eV) and using the Fermi level value (-5.57 eV) from Kelvin probe measurements, i.e. $E_{VBM} = E_f - 2.63$ eV = -8.2 eV. The corresponding conduction band edge was also found adding the value of the measured bandgap energy to the valence band edge, yielding a value of -3.93 eV.

We have recorded emission spectra of ZnO QDs at UV excitation wavelength 230 nm as shown in figure 8(a). Inset shows the emission spectra of same sample after eighteen months. ZnO generally shows photoluminescence in the UV and visible region. Figure 8(b) is a schematic diagram depicting this emission behavior in three different systems, that is, bulk ZnO, ZnO QDs and hydroxy-passivated ZnO QDs. Blue and green arrows in figure 8(b) point at the origin of UV and visible emissions, respectively. For bulk ZnO, the emission generally corresponds to different zinc and oxygen defects [48–50]. In particular, visible emission is often described in terms of recombination of conduction band electrons with deep-trap holes or recombination of electrons

present in near-conduction band traps with holes in the valance band [51]. The emission behavior in QDs, however, largely depends on the size of the QDs and quantum confinement regime. As the particle size reduces, the intensity of the UV emission generally increases without affecting the visible emission as shown in figure 8(b) for the ZnO QDs [52]. Our PL spectrum shows only UV emission without any peak in the visible range (figure 8(b), OH-ZnO QDs) that again corroborates defect-free ZnO QDs.

The main PL emission peak close to 330–340 nm and the corresponding Stokes shift (i.e. the difference between the onset of the absorption and the maximum of the PL emission spectra) is >200 meV. Experimentally, there have been many reports on significant Stokes shifts in many quantum dots e.g. CdSe [53], PbS [54] etc. A Stokes shift from 60 meV to 180 meV has been reported in ZnO nanorods with diameters decreasing from 14.5 nm to 6.5 nm, so that the shift observed in our measurements for the prominent peak at ~ 330 –340 nm is consistent with our mean diameter of 1.9 nm. The reason for a higher Stokes shift is related to enhancement of exciton localization in smaller particles [55].

Deconvolution of the PL emission spectrum shows a number of UV emission peaks (300 nm, 334 nm, 357 nm and 386 nm), figure 8(a). The small peak at 300 nm (4.13 eV) is related to confined excitonic emission. Also present is a prominent peak at 334 nm (3.71 eV) with two other peaks at 357 nm (3.47 eV) and 386 nm (3.21 eV) which are red shifted with respect to the excitonic emission.

Fonoberov *et al* have shown theoretically that when an surface bound ionized acceptor-exciton complex is present in the system [20], the position of the UV peak (334 nm) is hundreds of meV lower in energy than that for the confined exciton. Another possible reason is that the emission originate from exciton localization [55].

The emission at 357 nm (3.47 eV) and 386 nm (3.21 eV) on the other hand could be due to the strong molecular interaction of OH with Zn surface defects which introduce extra bands close to the conduction/valence band edges as shown in figure 8(b), OH-ZnO QDs. Furthermore, the strong interaction between empty Zn 3d, 4s and 4p molecular orbital and O lone-pair orbital of OH was observed in other reports where UV photoelectron spectroscopy results showed an increase of the emission in the area between the Zn 4s/O 2p and the Zn 3d band and a redistribution of the emission in the O 2p band was observed [56, 57].

Overall the PL analysis supports our material characterization where typical emission due to defects is not observed and where emission at 334 nm can be ascribed to OH-terminations, which is consistent with our chemical analysis. This confirms the formation of defect-free OH-passivated ZnO QDs.

In some cases reported in the literature [14], OH was observed on the surface of ZnO QDs; however this was clearly due to adsorbed water as they could not confirm Zn-OH bonding and their observation of visible emission indicated that OH did not contribute to surface defect passivation. Because of the strong confinement and very small size of QDs, the surface is normally highly reactive as a result of

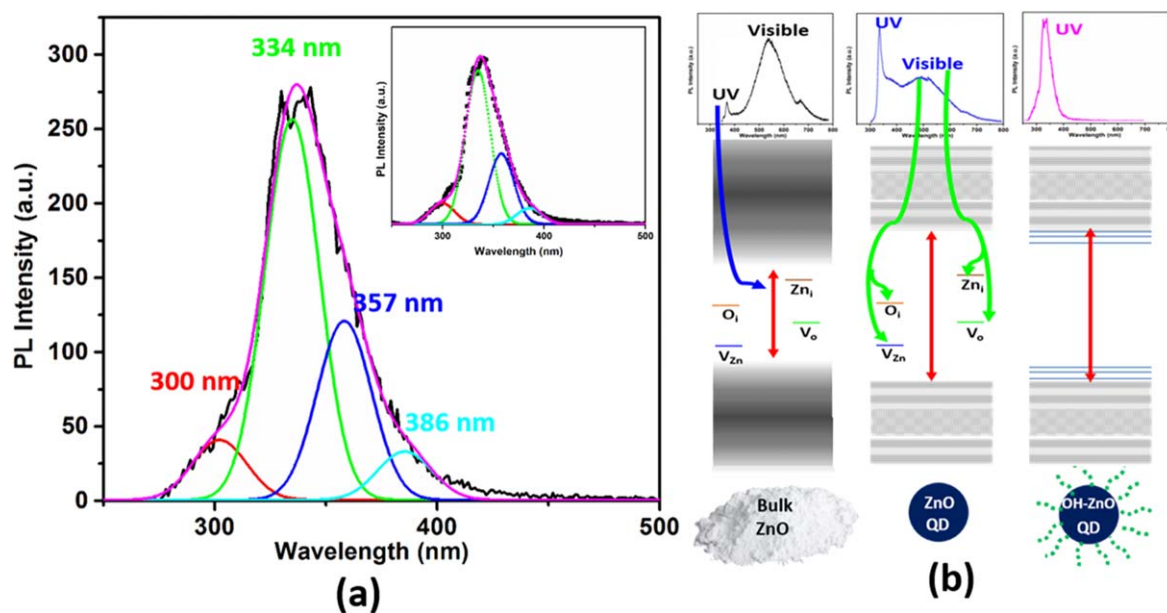


Figure 8. Photoluminescence spectra of ZnO QD shows (a) emission at 230 nm excitation wavelength and inset shows emission after eighteen-month (b) a comparative representation of band structure in bulk ZnO, ZnO QD and hydroxide passivated ZnO QD. Arrows illustrate the different emission mechanisms corresponding to UV and visible region.

the high density of surface O- and Zn-based defects, which can also contribute to surface degradation and changes in the opto-electronic properties. Many different approaches have been used to passivate these surface defects to reduce the visible emission contribution [11, 12]. However, these were generally post-synthesis methods. In our process, OH terminations are formed during synthesis which allows the formation of Zn–OH bonds within the plasma environment. The absence of any visible emission suggests the stabilization of surface defects, which is not the result of post-synthesis passivation.

4. Conclusion

We have shown a simple method to synthesize hydroxy-passivated ZnO QDs by non-thermal atmospheric pressure plasma which is unique and very simple in terms of managing precursors and its operation. Further, we investigated size and crystal structure by TEM to confirm wurtzite ZnO crystal structure and the absence of Zn(OH)₂. Our work report on the smallest ZnO QDs produced so far, with average diameter of 1.9 nm. The increase in bandgap is due to the strong confinement effect at this small size. The PL study reveals interesting aspects of these defect-free QDs where the emission spectra is limited to the UV region; this is the result of the introduction of energy states near to conduction and valence band edges, which removes O- and Zn-based defects that would normally lead to deeper trap states. This observation is further supported with the FTIR and XPS analysis where the OH bonding on the surface is confirmed. These OH-terminated ZnO QDs exhibit a stable PL emission for over the period of more than 18 months. This again supports our claim of OH termination, because of the OH-bonding on

the surface of the QDs do not migrate into the lattice structure and preserve their emission properties for very long time. This unique property can be promising for many emission related applications.

Acknowledgments

This work was supported by EPSRC awards (EP/M024938/1 and EP/K022237/1).

ORCID iDs

Gunisha Jain <https://orcid.org/0000-0003-4091-9356>

References

- [1] Huang M H, Mao S, Feick H, Yan H Q, Wu Y Y, Kind H, Weber E, Russo R and Yang P D 2001 Room-temperature ultraviolet nanowire nanolasers *Science* **292** 1897–9
- [2] Mitra A, Thareja R and Ganesan V 2001 Synthesis and characterization of ZnO thin films for UV laser *Appl. Surf.* **174** 232–9
- [3] Weintraub B, Wei Y, Wang Z L, Weintraub B, Wei Y and Wang Z L 2009 Optical fiber/nanowire hybrid structures for efficient three-dimensional dye-sensitized solar cells *Angew. Chem.—Int. Ed.* **48** 8981–5
- [4] Wei Y, Xu C, Xu S, Li C, Wu W and Wang Z L 2010 Planar waveguide-nanowire integrated three-dimensional dye-sensitized solar cells *Nano Lett.* **10** 2092–6
- [5] Law M, Greene L E, Johnson J C, Saykally R Y and D P 2005 Nanowire dye-sensitized solar cells *Nat. Mater.* **4** 445–59
- [6] Lévy-Clément C, Tena-Zaera R, Ryan M A, Katty A and Hodes G 2005 CdSe-sensitized p-CuSCN/nanowire n-ZnO heterojunctions *Adv. Mater.* **17** 1512–5

- [7] Pearton S J and Ren F 2014 Advances in ZnO-based materials for light emitting diodes *Curr. Opin. Chem. Eng.* **3** 51–5
- [8] Park W I and Yi G C 2004 Electroluminescence in n-ZnO nanorod arrays vertically grown on p-GaN *Adv. Mater.* **16** 87–90
- [9] Johnston K, Henry M O, McCabe D, McGlynn E, Dietrich M, Alves E and Xia M 2006 Identification of donor-related impurities in ZnO using photoluminescence and radiotracer techniques *Phys. Rev. B* **73** 1–7
- [10] Fonoberov V A, Alim K A, Balandin A A, Xiu F and Liu J 2006 Photoluminescence investigation of the carrier recombination processes in ZnO quantum dots and nanocrystals *Phys. Rev. B* **73** 1–9
- [11] Guo L, Yang S, Yang C, Yu P, Wang J, Ge W and Wong G K L 2000 Highly monodisperse polymer-capped ZnO nanoparticles: Preparation and optical properties *Appl. Phys. Lett.* **76** 2901
- [12] Djurišić A B et al 2004 Photoluminescence and electron paramagnetic resonance of ZnO tetrapod structures *Adv. Funct. Mater.* **14** 856–64
- [13] Patra M K, Manoth M, Singh V K, Gowd G S, Choudhry V S, Vadera S R and Kumar N A 2009 Synthesis of stable dispersion of ZnO quantum dots in aqueous medium showing visible emission from bluish green to yellow *J. Lumin.* **129** 320–4
- [14] Felbier P, Yang J, Theis J, Liptak R W, Wagner A, Lorke A, Bacher G and Kortshagen U 2014 Highly luminescent ZnO quantum dots made in a nonthermal plasma *Adv. Funct. Mater.* **24** 1988–93
- [15] Brookes I M, Murny C A and Thornton G 2001 Imaging water dissociation on TiO₂(110) *Phys. Rev. Lett.* **87** 266103–1–4
- [16] Schaub R, Thosttrup P, Lopez N, Lægsgaard E, Stensgaard I, Nørskov J K and Besenbacher F 2001 Oxygen vacancies as active sites for water dissociation on rutile TiO₂(110) *Phys. Rev. Lett.* **87** 266104–1–4
- [17] Kunat M, Girol S G, Burghaus U and Wöll C 2003 The interaction of water with the oxygen-terminated, polar surface of ZnO *J. Phys. Chem. B* **107** 14350–6
- [18] Fonoberov V A and Balandin A A 2004 Radiative lifetime of excitons in ZnO nanocrystals: the dead-layer effect *Phys. Rev. B* **70** 1–5
- [19] Shu-Lin Z 2012 *Raman Spectroscopy and its Application in Nanostructures* (New York: Wiley)
- [20] Fonoberov V A and Balandin A A 2004 Origin of ultraviolet photoluminescence in ZnO quantum dots: confined excitons versus surface-bound impurity exciton complexes *Appl. Phys. Lett.* **85** 5971–3
- [21] Fonoberov V A and Balandin A A 2006 ZnO quantum dots: physical properties and optoelectronic applications *J. Nanoelectron. Optoelectron.* **1** 19–38
- [22] Wang N, Yang Y and Yang G 2011 Great blue-shift of luminescence of ZnO nanoparticle array constructed from ZnO quantum dots *Nanoscale Res. Lett.* **6** 338
- [23] Gu Y, Kuskovsky I L, Yin M, O'Brien S and Neumark G F 2004 Quantum confinement in ZnO nanorods *Appl. Phys. Lett.* **85** 3833–5
- [24] Jain G, Macias-Montero M, Velusamy T, Maguire P and Mariotti D 2017 Porous zinc oxide nanocrystalline film deposition by atmospheric pressure plasma: fabrication and energy band estimation *Plasma Process. Polym.* **14** 1700052
- [25] Thi V H and Lee B 2017 Effective photocatalytic degradation of paracetamol using La-doped ZnO photocatalyst under visible light irradiation *Mater. Res. Bull.* **96** 171–82
- [26] Pang B, Yan J, Yao L, Liu H, Guan J, Wang H and Liu H 2016 Preparation and characterization of antibacterial paper coated with sodium lignosulfonate stabilized *RSC Adv.* **6** 9753–9
- [27] Mohan J 2004 *Organic Spectroscopy: Principles and Applications* (New Delhi: Narosa Publishing House Pvt)
- [28] Falk M 1984 The frequency of the HOH bending fundamental in solids and liquids *Spectrochim. Acta* **40** 43–8
- [29] Williams D H and Flemming I 2008 *Spectroscopy Methods In Organic Chemistry* (London: McGraw-Hill Higher Education)
- [30] Wang Y and Wöll C 2017 IR spectroscopic investigations of chemical and photochemical reactions on metal oxides: bridging the materials gap *Chem. Soc. Rev.* **46** 1875–932
- [31] McIntosh I M, Nichols A R L, Tani K and Llewellyn E W 2017 Accounting for the species-dependence of the 3500 cm⁻¹ H₂O infrared molar absorptivity coefficient: implications for hydrated volcanic glasses *Am. Mineral.* **102** 1677–89
- [32] Yaiphaba N, Ningthoujam R S, Singh N R and Vatsa R K 2010 Luminescence properties of redispersible Tb³⁺-doped GdPO₄ nanoparticles prepared by an ethylene glycol route *Eur. J. Inorg. Chem.* **2010** 2682–7
- [33] Nalawade S P, Picchioni F, Janssen L P B M, Grijpma D W and Feijen J 2008 Investigation of the interaction of CO₂ with poly(L-lactide), poly(DL-lactide) and poly(ϵ -caprolactone) using FTIR spectroscopy *J. Appl. Polym. Sci.* **109** 3376–81
- [34] Ramgir N S, Late D J, Bhise A B, More M A, Mulla I S, Joag D S and Vijayamohan K 2006 ZnO multipods, submicron wires, and spherical structures and their unique field emission behavior *J. Phys. Chem. B* **110** 18236–42
- [35] Wang M, Ren F, Zhou J, Cai G, Cai L, Hu Y, Wang D, Liu Y, Guo L and Shen S 2015 N Doping to ZnO nanorods for photoelectrochemical water splitting under visible light: engineered impurity distribution and terraced band structure *Sci. Rep.* **5** 12925
- [36] Alshammari A S, Chi L, Chen X, Bagabas A, Kramer D, Alromaeih A and Jiang Z 2015 Visible-light photocatalysis on C-doped ZnO derived from polymer-assisted pyrolysis *RSC Adv.* **5** 27690–8
- [37] Wang H, Baek S, Song J, Lee J and Lim S 2008 Microstructural and optical characteristics of solution-grown Ga-doped ZnO nanorod arrays *Nanotechnology* **19** 075607
- [38] Singh V P and Rath C 2015 Passivation of native defects of ZnO by doping Mg detected through various spectroscopic techniques *RSC Adv.* **5** 44390–7
- [39] Strohmeier B R and Hercules D M 1984 Characterization of the interaction zinc ions and γ -Alumina *J. Catal.* **86** 266–79
- [40] Ghosh S, Goudar V S, Padmalekha K G, Bhat S V, Indi S S and Vasani H N 2012 ZnO/Ag nanohybrid: synthesis, characterization, synergistic antibacterial activity and its mechanism *RSC Adv.* **2** 930
- [41] Scanlon M D, Peljo P, Méndez M A, Smirnov E and Girault H H 2015 Charging and discharging at the nanoscale: fermi level equilibration of metallic nanoparticles *Chem. Sci.* **6** 2705–20
- [42] Jakob M, Levanon H and Kamat P V 2003 Charge distribution between UV-irradiated TiO₂ and gold nanoparticles: Determination of shift in the Fermi level *Nano Lett.* **3** 353–8
- [43] Pesika N S, Stebe K J and Seanson P C 2003 Determination of the particle size distribution of quantum nanocrystals from absorbance spectra *Adv. Mater.* **15** 1289–91
- [44] Hybertsen M S 1994 Absorption and emission of light in nanoscale silicon structures *Phys. Rev. Lett.* **72** 1514–7
- [45] Efron A L and Rosen M 2000 The electronic structure of semiconductor nanocrystals *Annu. Rev. Mater. Sci.* **30** 475–521
- [46] Jacobsson T J and Edvinsson T 2011 Absorption and fluorescence spectroscopy of growing ZnO quantum dots: Size and band gap correlation and evidence of mobile trap states *Inorg. Chem.* **50** 9578–86
- [47] Bürkle M, Lozac'h M, McDonald C, Mariotti D, Matsubara K and Švrček V 2017 Bandgap engineering in OH-functionalized silicon nanocrystals: interplay between

- surface functionalization and quantum confinement *Adv. Funct. Mater.* **27** 1–7
- [48] Schejn A, Frégnaux M, Commenge J, Balan L, Falk L and Schneider R 2014 Size-controlled synthesis of ZnO quantum dots in microreactors *Nanotechnology* **25** 145606
- [49] Guo L, Yang S, Yang C, Yu P, Wang J, Ge W and Wong G K L 2000 Highly monodisperse polymer-capped ZnO nanoparticles: preparation and optical properties *Appl. Phys. Lett.* **76** 2901–3
- [50] Zhang L, Yin L, Wang C, Qi Y and Xiang D 2010 Origin of visible photoluminescence of ZnO quantum dots: defect-dependent and size-dependent *J. Phys. Chem. C* **114** 9651–8
- [51] Xiong H-M 2010 Photoluminescent ZnO nanoparticles modified by polymers *J. Mater. Chem.* **20** 4251
- [52] Fonoberov V A, Alim K A, Balandin A A, Xiu F and Liu J 2006 Photoluminescence investigation of the carrier recombination processes in ZnO quantum dots and nanocrystals *Phys. Rev. B* **2006** 1–9
- [53] Chen Z, Hellstr S, Ning Z, Yu Z and Fu Y 2011 Exciton polariton contribution to the Stokes shift in colloidal quantum dots *J. Phys. Chem. C* **115** 5286–93
- [54] Xu F, Gerlein L F, Ma X, Haughn C R, Doty M F and Cloutier S G 2015 Impact of different surface ligands on the optical properties of PbS quantum dot solids *Materials* **8** 1858–70
- [55] Lu J G, Ye Z Z, Zhang Y Z, Liang Q L, Fujita S and Wang Z L 2006 Self-assembled ZnO quantum dots with tunable optical properties *Appl. Phys. Lett.* **89** 4–6
- [56] Zwicker C and Jacobi K 1983 Site-specific interaction of H₂O with ZnO single-crystal surfaces studied by thermal desorption and UV photoelectron spectroscopy *Surf. Sci.* **131** 179–94
- [57] Cox P A H V 1994 *The Surface Science of Metal Oxides* vol 1994 (New York: Cambridge University Press)